CCS Chemistry

RESEARCH ARTICLE

Received: May 8, 2021 | Accepted: July 12, 2021

Bionic Thermosensation Inspired Temperature Gradient Sensor Based on Covalent Organic Framework Nanofluidic Membrane with Ultrahigh Sensitivity

Weipeng Xian[1†], Pengcheng Zhang[1†], Changjia Zhu[2], Xiuhui Zuo[1], Shengqian Ma[2*] & Qi Sun[1*]

[1]*Zhejiang Provincial Key Laboratory of Advanced Chemical Engineering Manufacture Technology, College of Chemical and Biological Engineering, Zhejiang University, Hangzhou 310027,* [2]*Department of Chemistry, University of North Texas, Denton, TX 76201*

**Corresponding authors: sunqichs@zju.edu.cn; shengqian.ma@unt.edu;* [†]W. Xian and P. Zhang contributed equally to this work.

Cite this: *CCS Chem.* **2021**, *3*, 2464–2472

The ability to precisely monitor temperature at a high resolution is an important task, particularly in terms of safety. Inspired by natural thermosensitive transient receptor potential cation channels, we developed a temperature sensor based on thermal-driven ionic charge separation. To mimic the function of nature, an ionic covalent organic framework-based nanofluidic membrane was fabricated. By engineering the membrane to separate two electrolyte solutions, the temperature difference across the membrane can synchronously induce a potential. The high charge density and narrow channel size render extraordinary permselectivity to the membrane, thus offering a thermosensation selectivity of up to 1.25 mV K^{-1}, superior to that of any known natural system. Additionally, the generated potential is linearly related to the introduced temperature gradient, thus allowing for precise detection. With these attributes, an alarm device with high thermosensation sensitivity was constructed, demonstrating great promise for environmental temperature monitoring.

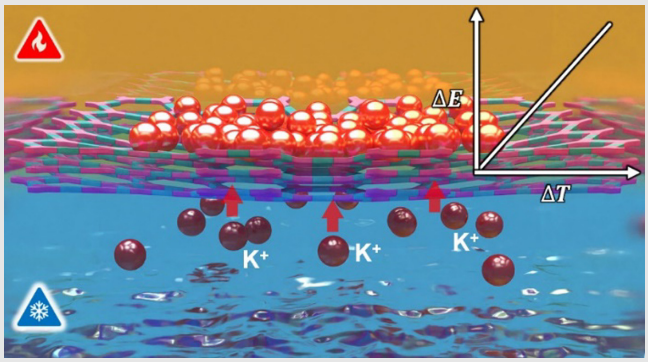

Keywords: **covalent organic framework, nanofluidic membrane, thermosensation, ionic charge separation, temperature monitoring**

Introduction

Temperature is one of the fundamental parameters in science and engineering.[1-3] Respective sensors are ubiquitous in daily life and in almost all industrial processes. It is estimated that temperature sensors occupy ~80% of the worldwide sensor market.[4-6] The physicochemical underpinnings of the current thermal sensation systems include (1) thermometers based on the thermal expansion of encased liquids, (2) optical sensors

DOI: 10.31635/ccschem.021.202101125
CCS Chem. **2021**, *3*, 2464–2472

based on thermochromic color switching, and (3) thermocouples based on the Seebeck effect. Given the synchronization and precision of thermoelectric conversion, thermocouples have become the most widely used industrial sensors.[7] However, the tremendous impact of the electromagnetic field on the movement of electrons and the directionality of temperature measurement (from hot to cold ends) limit their wide applications, thus calling for advanced techniques and materials for monitoring temperature.

Nature is the source of principle and functional innovation, inspiring scientists to develop sophisticated functional systems. Adaptive evolution has resulted in the development of specialized temperature-sensing mechanisms, enabling organisms to perceive subtle temperature stimuli rapidly. In mammals, this role is performed by a specialized family of membrane proteins containing transient receptor potential (TRP) channels, whose gating is sensitive to temperature variation.[8,9] The molecular basis of sensory perception is the thermal-driven ionic charge separation that ultimately results in an electrochemical potential difference. However, the fragility of the lipid bilayer diminishes the prospects for developing practical sensors using this technology. Recent significant theoretical and experimental advances in the nanofluidic field have enabled the replication of the functions of biological channels,[10–20] providing a potential opportunity to generate a new type of thermosensation device.[21–31] However, effectively regulating the thermophoretic mobilities of cations and anions over a wide concentration range of salt solutions remains a challenge. In addition, thermoelectric voltage under confinement is positively proportional to the surface charge density of the channel when the pore diameter is smaller or comparable with the thickness of the electric double layer (EDL).[32] This set of prerequisites necessitates the high-precision nanoscale design of ion channels from materials exhibiting high intrinsic charge density.

Covalent organic frameworks (COFs) are regular open matrices linked by organic struts.[33–45] In two-dimensional (2D) COFs, the layered sheets are stacked face-to-face in the third dimension, forming continuous transport channels. With such stunning structures, these materials have received considerable attention in the material community. The practicality of COFs in comparison with other materials for the design of nanofluidic membranes comes from their purely organic composition, which provides stability. Additionally, the monomer design can be fine-tuned due to the endless number of organic reactions at a chemist's disposal, resulting in a material that retains its robustness while providing a large number of available functional groups in nanospaces.[46–54] In this contribution, we demonstrate that COFs possess all the necessary traits for the design of high-performance thermosensation devices based on thermal-driven ionic charge separation. To address this challenging topic, a carboxylic acid-functionalized COF membrane (COF-COOH) was fabricated by pairing 1,3,5-triformylphloroglucinol (Tp) and 2,5-diaminobenzoic acid (Dba). Owing to its ultrasmall one-dimensional channel size (1.2 nm) and highly negatively charged surface, the resulting membrane was highly permselectivity, screening the transport of anions while favoring that of cations, thereby leading to significant transmembrane potentials in response to temperature gradients with a sensitivity of up to 1.25 mV K^{-1} (Figure 1). In addition, the thermoelectric response was rapid, stable, reproducible, and reversible, thus providing an alternative option for constructing a temperature monitoring system.

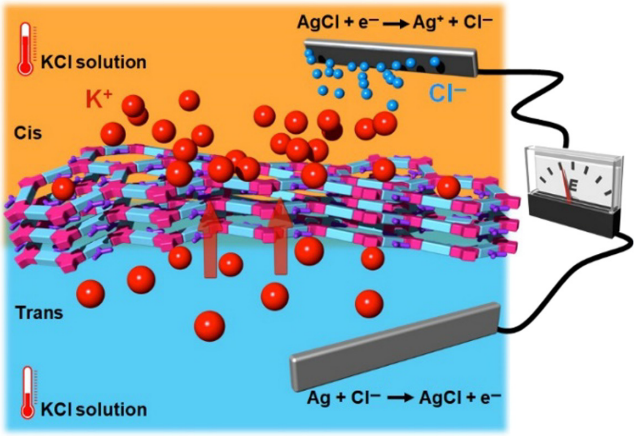

Figure 1 | *Schematic illustration of the thermoelectric conversion principle based on temperature gradient triggered transmembrane ionic charge separation.*

Experimental Methods

Fabrication of the free-standing COF-COOH membrane

The free-standing COF-COOH membrane was synthesized via interface condensation of Tp and Dba. The Dba (36.0 mg, 0.236 mmol) dispersed in a *p*-toluene sulfonic acid (TsOH, 89.8 mg, 0.472 mmol) aqueous phase (20 mL) was gently placed on top of the Tp (33.1 mg, 0.157 mmol) dichloromethane (20 mL) solution. The system was kept at 35 °C for 3 days. The free-standing COF-COOH was obtained as a brown powder after being washed thoroughly with water and ethanol in sequence and then dried under vacuum for further characterization.

Fabrication of COF-COOH/PAN

COF active layers were formed via interface polymerization on the surface of an asymmetric polyacrylonitrile

DOI: 10.31635/ccschem.021.202101125
CCS Chem. **2021**, *3*, 2464–2472

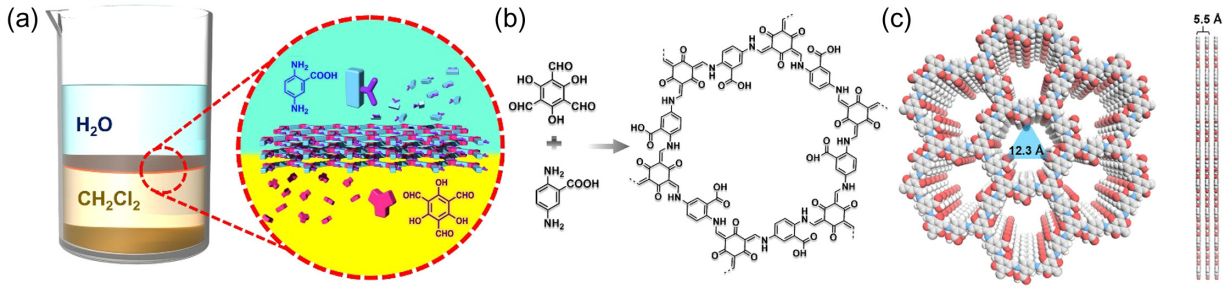

Figure 2 | *Fabrication of membrane. (a) Schematic illustration of the free-standing COF-COOH membrane by the interfacial polymerization of Tp and Dba in the presence of p-toluene sulfonic acid. (b) Synthetic scheme of COF-COOH. (c) Graphic views of the eclipsed stacking structure of COF-COOH (blue: N; gray: C; red: O; white: H).*

(PAN) ultrafiltration membrane. The PAN support was vertically placed in the middle of a homemade diffusion cell, resulting in a volume of 7 cm^3 in each cell (Supporting Information Figure S1). An aqueous solution of Dba (12.6 mg, 0.083 mmol) and TsOH (31.5 mg, 0.165 mmol) (7 mL) and the CH_2Cl_2 solution (7 mL) of Tp (11.6 mg, 0.055 mmol) were separately introduced into the two sides of the diffusion cell. The reaction mixture was kept at 35 °C for 3 days. The resulting membrane was rinsed with methanol to remove any residual monomers and catalyst. Finally, each membrane was rinsed with water for 24 h and then used for tests or air-dried for physicochemical characterization.

Results and Discussion

Nanofluidic membrane fabrication and characterization

The free-standing COF-COOH membrane was synthesized by interfacial polymerization, as depicted in Figure 2a, whereby the Dba dispersed in the TsOH aqueous phase was gently placed on top of the Tp dichloromethane solution (Figure 2b). The structure and crystallinity of the resulting COF membrane were scrutinized by powder X-ray diffraction (PXRD). The diffraction peak of 4.54° at 2θ is ascribed to the (100) plane of COF-COOH. The appearance of a characteristic peak of 26.6°at 2θ, attributable to the (001) plane, suggests the preferential planar orientation of the 2D sheets in the membrane (Supporting Information Figure S2). The experimental PXRD profile displays only limited deviations from the eclipsed stacking mode (Figure 2c and Supporting Information Table S1). The intensity of the diffraction peaks remained unchanged after treatment with 3M KCl, indicating the excellent salinity tolerance of COF-COOH, which is critical for using in a wide concentration range of salt solutions (Supporting Information Figure S2). The permanent porosity and pore size of the COF-COOH membrane were evaluated by N_2 sorption isotherms, which exhibited typical type-I reversible isotherms, characteristic of a microporous structure (Supporting Information Figure S3). The Brunauer–Emmett–Teller (BET) surface area was estimated to be 399 $m^2 g^{-1}$. Fitting of the sorption isotherms using the nonlocal density functional theory (NLDFT) model resulted in a pore size distribution centered at 1.2 nm, in conformity with the predicted value of the eclipsed stacking model. The zeta potential of COF-COOH is –11.6 ± 2.4, validating its highly negatively charged surface.

To increase the operability and stability of the COF membrane, we grew the COF layer on PAN ultrafiltration membranes. PAN was selected because of its flexibility and hydrophilicity, which is not only easy to handle but also highly permeable to ions. To control the COF active layers exclusively on the PAN support, the Tp-dichloromethane solution and the Dba-TsOH aqueous solution were separately introduced into a homemade diffusion cell segregated by PAN into two chambers (Supporting Information Figure S1). Over 3 days, a vermilion film was formed on PAN facing the organic phase (COF-COOH/PAN, Supporting Information Figure S4). Primary characterization of the resulting membrane was thoroughly performed prior to the thermoelectric response study.

The Fourier-transform infrared (FT-IR) spectrum of COF-COOH/PAN revealed that the adsorption features of –NH_2 (~3300 cm^{-1}) and –CHO (~2880 and ~1650 cm^{-1}) for the monomers disappeared with concomitant emergence of a peak for C=C at 1562 cm^{-1}, indicating a high condensation degree of the membrane and no mono mer being trapped in the pore channel (Supporting Information Figure S5).[55] Scanning electron microscopy (SEM) images revealed continuous film surfaces that contoured the underlying PAN support with a thickness of approximately 220 nm (Supporting Information Figures S6 and S7). Contact angle measurements revealed that COF-COOH/PAN was hydrophilic with a water contact angle of 52 ± 4° (Supporting Information Figure S8). Dye molecule exclusion tests indicated that the COF active layer is porous but without large defects because the negatively charged thymol blue, with size (1.0 × 1.1 nm),

DOI: 10.31635/ccschem.021.202101125
CCS Chem. **2021**, *3*, 2464–2472

penetrated the membrane, whereas methyl blue, with a greater size (1.5 × 2.0 nm), was fully withheld (see details in the Experimental Section in the Supporting Information Figure S9).

Ion permselectivity evaluation

Encouraged by these characterization results, we next investigated the ion transport properties of COF-COOH/PAN. Given the similar bulk diffusivities of K^+ and Cl^-, KCl was the electrolyte of choice (unbuffered KCl was used unless otherwise specified). COF-COOH/PAN was located between the two chambers of a conductivity cell. The transmembrane current was recorded using symmetric KCl solutions with concentrations ranging from 0.01 mM to 3 M (Supporting Information Figure S10). The variation of the normalized transmembrane conductance derived from the slope of the current–voltage (*I*–*V*) curve versus KCl concentrations confirmed the nanoscale channels and the absence of KCl leakage through large cracks (Figure 3a). Ions were transported across COF-COOH/PAN in a fashion parallel to that in the bulk electrolyte at high electrolyte concentrations (>100 mM). At lower ionic strengths (<100 mM), the ion conductivity of COF-COOH/PAN deviated from the bulk behavior and demonstrated saturation, which is typical of surface-charge-governed ionic transport. Under such circumstances, the electrostatic force of the overlapped EDL could screen ions, repel co-ions, and attract counter-ions. Moreover, considering that the surface-charge-governed regime of COF-COOH/PAN extended above 100 mM, under which the Debye screening lengths was around 1 nm (Supporting Information Table S2), we can therefore conclude that the pore size of the membrane is smaller than 2 nm. These results further validate that there are no big cracks in the membrane.[56]

To quantitatively evaluate the permselectivity of COF-COOH/PAN, its reversal potentials (V_r) under various KCl concentration gradients were evaluated. To do so, COF-COOH/PAN was mounted between asymmetric KCl solutions, with one side facing the COF active layer, denoted as the cis side, and the other side named as the trans side. The x-intercepts (V_r) of the *I*–*V* plots exhibited average reversal potentials (three times) of –58.4, –112.4, and –109.6 mV for cis/trans = 1.0/0.1, 10/0.1, and 100/0.1 mM KCl, respectively (Figure 3b). The permeability ratios of K^+/Cl^- calculated based on the Goldman equation (eq 1) were 449, 416, and 78, respectively, confirming the preferential passage of cations over a wide range of concentration gradients.[57]

$$\frac{P_{K^+}}{P_{Cl^-}} = \frac{a_{Cl^-,cis} \cdot \exp(-V_r F/RT) - a_{Cl^-,trans}}{a_{K^+,cis} - a_{K^+,trans} \cdot \exp(-V_r F/RT)} \quad (1)$$

To gain additional insight into the ion transport profiles inside the nanopores, theoretical calculations using a continuum approach based on the Nernst–Planck–Poisson equations were performed using COMSOL. The calculation model is illustrated in the Supporting Information Figure S11, whereby a negatively charged nanochannel separates KCl solutions with different concentration gradients. The dimension of the nanochannel was set according to the characterization results (200 nm length and 1.2 nm diameter). To gain affordable computation scale, a 2D model was employed and the fluidic pathway was simplified to be a 200 nm long single channel with a width of 1.2 nm. The radial ion distribution from the channel axis to the channel wall was calculated, which revealed the presence of high concentration of K^+ ions throughout the channel, even at low bath concentrations. Moreover, the concentration of Cl^- ions was always lower than that of K^+ ions, although the discrepancy decreased with an increase

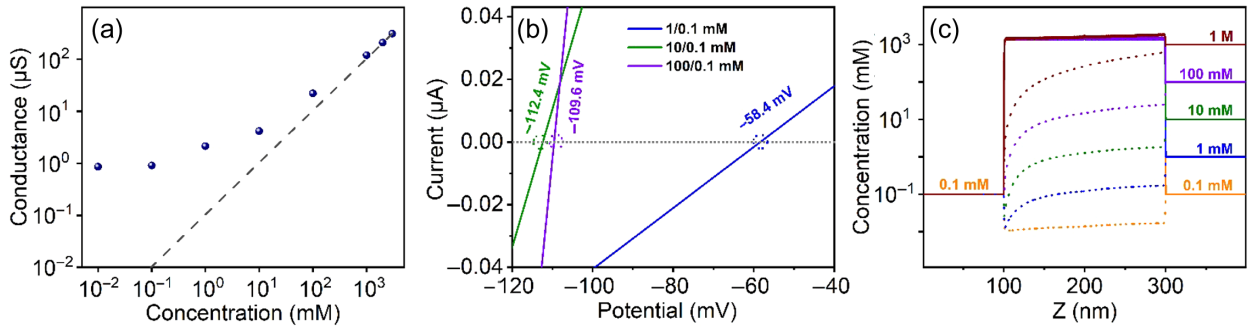

Figure 3 | *Investigation of transmembrane ion transport. (a) Measured steady-state ionic conductance of COF-COOH/PAN, as well as a bulk prediction for KCl solutions (dashed line). The bulk conductivity represents the conditions where the effect of the surface charge can be neglected. (b) I–V curves recorded under various KCl concentration gradients separated by COF-COOH/PAN. (c) Numerical simulation of the distributions of K^+ (solid line) and Cl^- (dashed line) with various concentration gradients (the left side was fixed at 0.1 mM, while the right side increased from 0.1 mM to 1 M) inside the nanochannels of COF-COOH.*

DOI: 10.31635/ccschem.021.202101125
CCS Chem. **2021**, *3*, 2464–2472

in the concentration gradient, consistent with the experimental results (Figure 3c). These phenomena can be rationalized by the high negative charge density and ultrasmall channel size of COF-COOH that produce co-ion exclusion.[58,59]

Theoretical principle of biomimetic thermosensation

Developments in the principles of nanofluidic transport allow us to mimic the function of biological pores. It is established that the transmembrane diffusion potential (ϕ_{diff}) is a function of temperature and salt activity of the electrolytes (eq 2 and see detailed derivation process in the Supporting Information), where t_+ is the transference number of cations, T is temperature, and a is the electrolyte activity.

$$\phi_{diff} = \phi_{cis} - \phi_{trans} = (2t_+ - 1)\frac{R}{F}(T_{trans} \ln a_{trans} - T_{cis} \ln a_{cis}) \quad (2)$$

Experimentally, we can measure the open-circuit potential (V_{oc}) directly. According to the equivalent circuit of our experimental setup, V_{oc} is the sum of ϕ_{diff}, the redox potential of the Ag/AgCl electrodes (E_{redox}), and the voltage drops across the membrane ($iR_{membrane}$) and solution ($iR_{solution}$), where i is the ionic current, and $R_{membrane}$ and $R_{solution}$ are the internal resistance of the membrane and the solution resistance, respectively (eq 3).

$$V_{oc} = V_{cis} - V_{trans} = -(\phi_{diff} + E_{redox} + iR_{membrane} + iR_{solution}) \quad (3)$$

E_{redox} can be calculated using eq 4.

$$E_{redox} = E_{cis} - E_{trans} = \frac{R}{F}(T_{trans} \ln a_{trans} - T_{cis} \ln a_{cis}) \quad (4)$$

Under open-circuit conditions, i is close to 0 and the drops in iR can be ignored. Therefore, the equation V_{oc} relating to the solution temperature and concentration can be established as eq 5.

$$V_{oc} = -(\phi_{diff} + E_{redox}) = -2t_+\frac{R}{F}(T_{trans} \ln a_{trans} - T_{cis} \ln a_{cis}) \quad (5)$$

To study the potential changes in response to the temperature gradients between the two electrolytes, we used symmetric solutions ($a_{cis} = a_{trans} = a$). Both ϕ_{diff} and V_{oc} are equal to zero at the initial state ($T_{cis} = T_{trans}$). Upon introducing a temperature gradient, ΔT ($\Delta T = |T_{trans} - T_{cis}|$), the magnitude of the potential changes can be derived from eqs 6 and 7.

$$\Delta V_{oc}(T) = -2t_+\frac{R}{F}\Delta T \ln a \quad (6)$$

$$\Delta \phi_{diff}(T) = (2t_+ - 1)\frac{R}{F}\Delta T \ln a \quad (7)$$

Thermoelectric response evaluation

Once we confirmed the high permselectivity of COF-COOH/PAN, we proceeded to study its thermoelectric response properties. To investigate the influence of the temperature gradient between the two chambers on the transmembrane potential, COF-COOH/PAN was placed in contact with symmetric KCl solutions (1 mM). In the steady state, negligible zero-voltage currents were detected. When a slight temperature gradient was induced by briefly heating or cooling one end of the solution, an apparent voltage was observed, suggesting the remarkable sensitivity of temperature-driven ion transport (Supporting Information Figure S12). To quantitatively study the thermoelectric response, a customized setup was engineered, whereby ΔT was recorded by a pair of immersed microthermometers, and the changes in voltage (ΔV_{oc}) were monitored by Ag/AgCl electrodes, which were output by an electrochemical workstation (Supporting Information Figure S13). Figure 4a depicts the time evolution curves of ΔT and ΔV_{oc} recorded with COF-COOH/PAN, during which the temperature of the trans side increased from 25 °C to approximately 35 °C and then returned naturally to thermal equilibrium, whereby ΔV_{oc} synchronously changed in response to temperature changes. In the cooling stage, both ΔV_{oc} and ΔT decreased with time, and vice versa. A linear dependence with a correlation coefficient (R^2) value greater than 0.99 was obtained by plotting the variation of V_{oc} against temperature changes, in line with the theoretical derivation (eq 6 and Figure 4a, inset). Averaging over three different batches, the thermosensation sensitivity derived from the slope of the aforementioned plots was 1.17 mV K^{-1} for COF-COOH/PAN, far outcompeting the thermosensation sensitivity of organisms as well as the reported systems (Supporting Information Table S3).[60–64] Moreover, this temperature-induced potential change was reversible and instantaneous, and no degradation of performance was observed for at least eight cycles, indicating a stable linear correlation between the temperature gradient and ion transport potential (Figure 4b and Supporting Information Table S4). Impressively, the device showed instantaneous response to the temperature stimuli, with an average relative sensitivity of 97% (see details in the Supporting Information Figure S14).

Given that ΔV_{oc} is independent of the initial temperature but not ΔT, we further investigated the thermosensation capability of COF-COOH/PAN. Initially, we evaluated the thermoelectric responses of the developed thermosensation system toward other temperature windows. The permselectivity of COF-COOH/PAN was

DOI: 10.31635/ccschem.021.202101125
CCS Chem. **2021**, *3*, 2464–2472

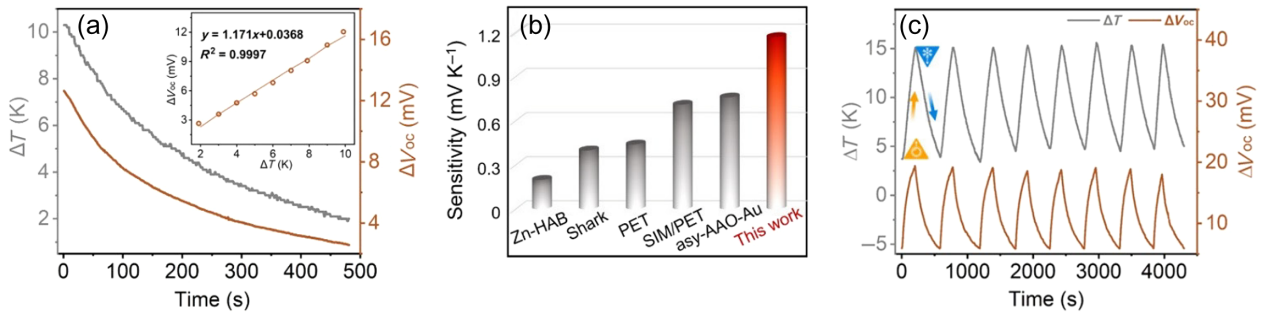

Figure 4 | *Thermosensation performance evaluation of COF-COOH/PAN. (a) The synchronous time evolution of ΔV_{oc} in response to the solution temperature change with the initial temperatures of 25 and 35 °C, respectively, inset: The linear fits of ΔV_{oc} against ΔT according to eq 6. (b) Comparison of thermosensation sensitivity for COF-COOH/PAN with those of other benchmark systems, ZnHAB;[60] Shark;[61] poly(ethylene terephthalate) PET;[62] silica isoporous nanochannels (SIM)/PET;[62] asy-AAO-Au.[63] (c) Continuous and synchronous time evolution curves of ΔV_{oc} (blue) and ΔT (red) recorded with COF-COOH/PAN membrane in 1 mM KCl for eight cycles.*

retained in response to both hot and cold stimuli. For example, the t_+ values for the systems within the temperature ranges of 15–25 °C and 35–45 °C were calculated to be 0.968 and 0.951, respectively. Moreover, linear relationships between ΔV_{oc} and ΔT were observed, giving rise to the thermosensation sensitivities of 1.16 and 1.14 mV K^{-1}, respectively, and manifesting its wide operating temperature windows (Supporting Information Figures S15 and S16).

To evaluate the performance of COF-COOH/PAN to track the temperature gradients of various environments, we investigated its thermoelectric response toward electrolytes with a wide range of concentrations. Similar profiles of ΔV_{oc} in response to ΔT were recorded. Linear expressions by plotting ΔV_{oc} against ΔT reflected the proportional potential difference to the temperature gradient under various ionic strengths (Supporting Information Figure S17). The thermoelectric sensitivities derived from the slopes were found to be in the range of 1.25–0.38 mV K^{-1} over KCl concentrations of 0.5–100 mM (Supporting Information Table S5). The sensitivities decreased with increasing electrolyte concentration, which can be reasonably explained by eq 6; the slope decreased as ln*a* increased. Furthermore, to evaluate the thermosensation properties of COF-COOH/PAN in the presence of salt concentration gradients, 0.5 M and 0.01 M KCl were used as electrolytes, which acted as surrogates of seawater and river water, respectively. After a brief heating was imposed on the low-salt side, a maximum V_{oc} value of 167.8 mV was detected, corresponding to the t_+ value of 0.985, which supported the high permselectivity of COF-COOH/PAN. Fitting the experimental results, a linear dependence of ΔV_{oc} and ΔT was also observed, showing a thermosensation sensitivity of 0.80 mV K^{-1} (Supporting Information Figure S18). Collectively, these results indicate the potential applicability of COF-COOH/PAN as a temperature sensor.

The thermosensation sensitivity behaviors of COF-COOH/PAN with other electrolyte were also evaluated, showing that the thermosensation sensitivity decreases in the order of KCl (1.17 mV K^{-1}) > NaCl (0.90 mV K^{-1}) > LiCl (0.85 mV K^{-1}). This can be rationalized by their difference in diffusion coefficient of cations, decreasing in the order K^+ > Na^+ > Li^+ (Supporting Information Figures S19 and S20). The faster the cation diffuses, the more efficient the charge separation will occur, which is a typical behavior of cation-selective membranes. The high thermosensation sensitivity of COF-COOH/PAN shows potential in harvesting low-quality temperature gradient into electricity. To do so, COF-COOH/PAN was placed between the asymmetric NaCl aqueous solutions (0.5/0.01 M) to mimic the salinity gradient at a river mouth. Given that the concentration gradient and hot stimulation drive the ion transport in opposite directions, the temperature gradient was imposed on the low-salt concentration side. The initial V_{oc} and I_{sc} values were measured to be 156.7 mV and 13.8 μA, respectively. Calculated according to $P_{out} = V_{oc} \times I_{sc}/4$, a power density of 68.7 W m^{-2} was obtained. After introducing a temperature gradient of approximately 15 K, the V_{oc} and I_{sc} values increased to 169.0 mV and 16.9 μA, respectively, and the power density was calculated to be 91.0 W m^{-2} (Supporting Information Figure S21).

Temperature alarm device

The high tolerance toward various conditions in terms of salt concentrations and temperature windows, as well as the ultrahigh thermosensation sensitivity of COF-COOH/PAN, motivated us to explore the possibilities of designing a temperature alarm system (Supporting Information Figure S22). As the magnitude of the voltage increases linearly with an increase in the temperature gradient, we could precisely set an alarm limit. To visualize the alarm

DOI: 10.31635/ccschem.021.202101125
CCS Chem. **2021**, *3*, 2464–2472

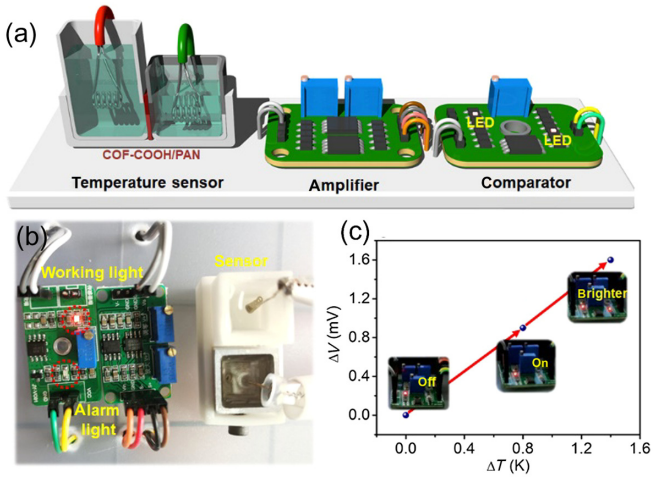

Figure 5 | *Application demonstration of the thermosensation system for the design of temperature alarm device. (a) Schematic diagram of the integral sensing system. (b) Photograph of the sensing and display system. (c) Dependence of the LED lamp brightness on temperature variations.*

signal, we assembled an integral system that can translate information about temperature gradient into voltage signals that are then taken up and amplified by a microcontroller unit (Figure 5a). The light-emitting diodes (LEDs) responded spontaneously when the change in temperature exceeded the predetermined alarm limit. Figure 5b shows a digital photograph of the experimental setup. To use as a sensor for monitoring the changes in the surrounding temperature, a conductivity cell made from different materials and volume was employed. Owing to the different thermal conductivities of aluminum and plastic materials, the temperature of electrolyte (0.1 mM KCl) in the plastic cell with large volume can be considered as unchanged in a short time when the surrounding environment temperature changes, but that in the aluminum cell with small volume does not. In a steady state, the potential between the two cells remains the same; thus, the output voltage is zero at the load resistance. When the surrounding temperature changes, a temperature gradient between the two chambers is formed, and the sensor outputs a voltage, which activates the alarm circuit that lights the LED after overriding the set limit. Given that the magnitude of the temperature gradient determines the value of the pulse voltage, the gating temperature can be precisely set by manipulating the circuit. Additionally, the ultrahigh thermosensation selectivity of the developed system allows a tiny temperature variation to be detected. To demonstrate a showcase study, we set the temperature gradient around 1 K as a safe variation. We heated or cooled the sensor and measured the temperature gradients to test the feasibility of the device. It was shown that when the temperature gradient of the electrolytes exceeded the safe value, the LED was lighted. Upon further increasing the temperature gradient, the lamp light intensity increased within a specific range (Figure 5c and Supporting Information Movies S1 and S2).

Conclusions

This work demonstrates one of the very first examples of using temperature as a precision input in a responsive membrane-based ionic charge separation system to obtain stable, reversible, and instant electrochemical signal output, with the attributes of ultrasensitivity and high tolerance toward various operating conditions. We advanced COF as a customized platform to mimic the function of thermo-transient receptor potential channels in nature with high performance; a thermosensation sensitivity of up to 1.25 mV K^{-1} was obtained, placing it within striking distance of the all-time temperature sensor record. We believe that introducing the developed thermosensation system to the compendium of realized temperature sensors can fill the current gap in temperature-responsive materials.

Supporting Information

Supporting Information is available and includes materials syntheses, characterization details, and supporting figures.

Conflict of Interest

There is no conflict of interest to report.

Funding Information

The authors acknowledge the National Science Foundation of China (no. 22072132). Partial support from the Robert A. Welch Foundation (no. B-0027) is also acknowledged (S.M.).

References

1. Lumpkin, E. A.; Caterina, M. J. Mechanisms of Sensory Transduction in the Skin. *Nature* **2007**, *445*, 858–865.
2. Vriens, J.; Nilius, B.; Voets, T. Peripheral Thermosensation in Mammals. *Nat. Rev. Neurosci.* **2014**, *15*, 573–589.
3. Chowdhury, S.; Jarecki, B. W.; Chanda, B. A Molecular Framework for Temperature-Dependent Gating of Ion Channels. *Cell* **2014**, *158*, 1148–1158.
4. Nirmala, A.; Mukkatt, I.; Shankar, S.; Ajayaghosh, A. Thermochromic Color Switching to Temperature Controlled Volatile Memory and Counter Operations with Metal-Organic Complexes and Hybrid Gels. *Angew. Chem. Int. Ed.* **2021**, *60*, 455–465.

5. Wang, X.-d.; Wolfbeis, O. S.; Meier, R. J. Luminescent Probes and Sensors for Temperature. *Chem. Soc. Rev.* **2013**, *42*, 7834–7869.
6. Childs, P. R. N.; Greenwood, J. R.; Long, C. A. Review of Temperature Measurement. *Rev. Sci. Instrum.* **2000**, *71*, 2959–2978.
7. Gambino, R. J.; Brook, S.; Longtin, J. P.; Jefferson, P.; Brogan, J. A.; Gutleber, J. A.; Beach, H.; Greenlaw, R. J. Thermocouples. U.S. Patent 7753584 B2, Jul. 13, **2010**.
8. Damann, N.; Voets, T.; Nilius, B. TRPs in Our Senses. *Curr. Biol.* **2008**, *18*, R880–R889.
9. Voets, T.; Droogmans, G.; Wissenbach, U.; Janssens, A.; Flockerzi, V.; Nilius, B. The Principle of Temperature-Dependent Gating in Cold- and Heat-Sensitive TRP Channels. *Nature* **2004**, *430*, 748–754.
10. Li, X.; Zhang, H.; Yu, H.; Xia, J.; Zhu, Y.-B.; Wu, H.-A.; Hou, J.; Lu, J.; Ou, R.; Easton, C. D.; Selomulya, C.; Hill, M. R.; Jiang, L.; Wang, H. Unidirectional and Selective Proton Transport in Artificial Heterostructured Nanochannels with Nano-to-Subnano Confined Water Clusters. *Adv. Mater.* **2020**, *32*, 2001777.
11. Lu, J.; Zhang, H.; Hou, J.; Li, X.; Hu, X.; Hu, Y.; Easton, C. D.; Li, Q.; Sun, C.; Thornton, A. W.; Hill, M. R.; Zhang, X.; Jiang, G.; Liu, J. Z.; Hill, A. J.; Freeman, B. D.; Jiang, L.; Wang, H. Efficient Metal Ion Sieving in Rectifying Subnanochannels Enabled by Metal-Organic Frameworks. *Nat. Mater.* **2020**, *19*, 767–774.
12. Shehzad, M. A.; Wang, Y.; Yasmin, A.; Ge, X.; He, Y.; Liang, X.; Zhu, Y.; Hu, M.; Xiao, X.; Ge, L.; Jiang, C.; Yang, Z.; Guiver, M. D.; Wu, L.; Xu, T. Biomimetic Nanocones that Enable High Ion Permselectivity. *Angew. Chem. Int. Ed.* **2019**, *131*, 12776–12784.
13. Tan, R.; Wang, A.; Malpass-Evans, R.; Williams, R.; Zhao, E. W.; Liu, T.; Ye, C.; Zhou, X.; Darwich, B. P.; Fan, Z.; Turcani, L.; Jackson, E.; Chen, L.; Chong, S. Y.; Li, T.; Jelfs, K. E.; Cooper, A. I.; Brandon, N. P.; Grey, C. P.; McKeown, N. B.; Song, Q. Hydrophilic Microporous Membranes for Selective Ion Separation and Flow-Battery Energy Storage. *Nat. Mater.* **2020**, *19*, 195–202.
14. Xu, Y. Nanofluidics: A New Arena for Materials Science. *Adv. Mater.* **2018**, *30*, 1702419.
15. Tagliazucchi, M.; Szleifer, I. Transport Mechanisms in Nanopores and Nanochannels: Can We Mimic Nature? *Mater. Today* **2015**, *18*, 131–142.
16. Jiang, Z.-Y.; Liu, H.-L.; Ahmed, S. A.; Hanif, S.; Ren, S.-B.; Xu, J.-J.; Chen, H.-Y.; Xia, X.-H.; Wang, K. Insight into Ion Transfer through the Sub-Nanometer Channels in Zeolitic Imidazolate Frameworks. *Angew. Chem. Int. Ed.* **2017**, *56*, 4767–4771.
17. Xiao, K.; Chen, L.; Zhang, Z.; Xie, G.; Li, P.; Kong, X.-Y.; Wen, L.; Jiang, L. A Tunable Ionic Diode Based on a Biomimetic Structure-Tailorable Nanochannel. *Angew. Chem. Int. Ed.* **2017**, *56*, 8168–8172.
18. Wang, J.; Zhang, Z.; Zhu, J.; Tian, M.; Zheng, S.; Wang, F.; Wang, X.; Wang, L. Ion Sieving by a Two-Dimensional $Ti_3C_2T_x$ Alginate Lamellar Membrane with Stable Interlayer Spacing. *Nat. Commun.* **2020**, *11*, 3540.
19. Ding, L.; Xiao, D.; Lu, Z.; Deng, J.; Wei, Y.; Caro, J.; Wang, H. Oppositely Charged $Ti_3C_2T_x$ MXene Membranes with 2D Nanofluidic Channels for Osmotic Energy Harvesting. *Angew. Chem. Int. Ed.* **2020**, *132*, 8798–8804.
20. Zhang, Z.; Yang, S.; Zhang, P.; Zhang, J.; Chen, G.; Feng, X. Mechanically Strong MXene/Kevlar Nanofiber Composite Membranes as High-Performance Nanofluidic Osmotic Power Generators. *Nat. Commun.* **2019**, *10*, 2920.
21. Arnott, P. M.; Howorka, S. A Temperature-Gated Nanovalve Self-Assembled from DNA to Control Molecular Transport across Membranes. *ACS Nano* **2019**, *13*, 3334–3340.
22. de la Escosura-Muñiz, A.; Merkoçi, A. Nanochannels Preparation and Application in Biosensing. *ACS Nano* **2012**, *6*, 7556–7583.
23. Bocquet, L.; Charlaix, E. Nanofludics, from Bulk to Interfaces. *Chem. Soc. Rev.* **2010**, *39*, 1073–1095.
24. Nasir, S.; Ali, M.; Ensinger, W. Thermally Controlled Permeation of Ionic Molecules through Synthetic Nanopores Functionalized with Amine-Terminated Polymer Brushes. *Nanotechnology* **2012**, *23*, 225502.
25. Reber, N.; Küchel, A.; Spohr, R.; Wolf, A.; Yoshida, M. Transport Properties of Thermo-Responsive Ion Track Membranes. *J. Membr. Sci.* **2001**, *193*, 49–58.
26. Yameen, B.; Ali, M.; Neumann, R.; Ensinger, W.; Knoll, W.; Azzaroni, O. Ionic Transport through Single Solid-State Nanopores Controlled with Thermally Nanoactuated Macromolecular Gates. *Small* **2009**, *5*, 1287–1291.
27. Zhang, Z.; Xie, G.; Xiao, K.; Kong, X.-Y.; Li, P.; Tian, Y.; Wen, L.; Jiang, L. Asymmetric Multifunctional Heterogeneous Membranes for pH- and Temperature-Cooperative Smart Ion Transport Modulation. *Adv. Mater.* **2016**, *28*, 9613–9619.
28. Ma, Y.; Centola, M.; Keppner, D.; Famulok, M. Interlocked DNA Nanojoints for Reversible Thermal Sensing. *Angew. Chem. Int. Ed.* **2020**, *59*, 12455–12459.
29. Zhou, Y.; Guo, W.; Cheng, J.; Liu, Y.; Li, J.; Jiang, L. High-Temperature Gating of Solid-State Nanopores with Thermo-Responsive Macromolecular Nanoactuators in Ionic Liquids. *Adv. Mater.* **2012**, *24*, 962–967.
30. Wang, R.; Sun, Y.; Zhang, F.; Song, M.; Tian, D.; Li, H. Temperature-Sensitive Artificial Channels through Pillar[5]arenebased Host-Guest Interactions. *Angew. Chem. Int. Ed.* **2017**, *56*, 5294–5298.
31. Huang, K.; Szleifer, I. Design of Multifunctional Nanogate in Response to Multiple External Stimuli Using Amphiphilic Diblock Copolymer. *J. Am. Chem. Soc.* **2017**, *139*, 6422–6430.
32. Dietzel, M.; Hardt, S. Thermoelectricity in Confined Liquid Electrolytes. *Phys. Rev. Lett.* **2016**, *116*, 225901.
33. Song, Y.; Sun, Q.; Aguila, B.; Ma, S. Opportunities of Covalent Organic Frameworks for Advanced Applications. *Adv. Sci.* **2019**, *6*, 1801410.
34. Slater, A. G.; Cooper, A. I. Function-Led Design of New Porous Materials. *Science* **2015**, *348*, aaa8075.
35. Lohse, M. S.; Bein, T. Covalent Organic Frameworks: Structures, Synthesis, and Applications. *Adv. Funct. Mater.* **2018**, *28*, 1705553.
36. Kandambeth, S.; Dey, K.; Banerjee, R. Covalent Organic Frameworks: Chemistry beyond the Structure. *J. Am. Chem. Soc.* **2019**, *141*, 1807–1822.

DOI: 10.31635/ccschem.021.202101125
CCS Chem. **2021**, *3*, 2464–2472

37. Jin, Y.; Hu, Y.; Zhang, W. Tessellated Multiporous Two-Dimensional Covalent Organic Frameworks. *Nat. Rev. Chem.* **2017**, *1*, 0056.
38. Han, X.; Yuan, C.; Hou, B.; Liu, L.; Li, H.; Liu, Y.; Cui, Y. Chiral Covalent Organic Frameworks: Design, Synthesis and Property. *Chem. Soc. Rev.* **2020**, *49*, 6248–6272.
39. Guan, X.; Chen, F.; Fang, Q.; Qiu, S. Design and Applications of Three Dimensional Covalent Organic Frameworks. *Chem. Soc. Rev.* **2020**, *49*, 1357–1384.
40. Geng, K.; He, T.; Liu, R.; Dalapati, S.; Tan, K. T.; Li, Z.; Tao, S.; Gong, Y.; Jiang, Q.; Jiang, D. Covalent Organic Frameworks: Design, Synthesis, and Functions. *Chem. Rev.* **2020**, *120*, 8814–8933.
41. Evans, A. M.; Parent, L. R.; Flanders, N. C.; Bisbey, R. P.; Vitaku, E.; Kirschner, M. S.; Schaller, R. D.; Chen, L. X.; Gianneschi, N. C.; Dichtel, W. R. Seeded Growth of Single-Crystal Two-Dimensional Covalent Organic Frameworks. *Science* **2018**, *361*, 52–57.
42. Liu, H.; Chu, J.; Yin, Z.; Cai, X.; Zhuang, L.; Deng, H. Covalent Organic Frameworks Linked by Amine Bonding for Concerted Electrochemical Reduction of CO_2. *Chem* **2018**, *4*, 1696–1709.
43. Dong, J.; Zhang, K.; Li, X.; Qian, Y.; Zhu, H.; Yuan, D.; Xu, Q.-H.; Jiang, J.; Zhao, D. Ultrathin Two-Dimensional Porous Organic Nanosheets with Molecular Rotors for Chemical Sensing. *Nat. Commun.* **2017**, *8*, 1142.
44. Colson, J. W.; Woll, A. R.; Mukherjee, A.; Levendorf, M. P.; Spitler, E. L.; Shields, V. B.; Spencer, M. G.; Park, J.; Dichtel, W. R. Oriented 2D Covalent Organic Framework Thin Films on Single-Layer Graphene. *Science* **2011**, *332*, 228–231.
45. Yang, Y.; Faheem, M.; Wang, L.; Meng, Q.; Sha, H.; Yang, N.; Yuan, Y.; Zhu, G. Surface Pore Engineering of Covalent Organic Frameworks for Ammonia Capture through Synergistic Multivariate and Open Metal Site Approaches. *ACS Cent. Sci.* **2018**, *4*, 748–754.
46. Valentino, L.; Matsumoto, M.; Dichtel, W. R.; Mariñas, B. J. Development and Performance Characterization of a Polyimine Covalent Organic Framework Thin-Film Composite Nanofiltration Membrane. *Environ. Sci. Technol.* **2017**, *51*, 14352–14359.
47. Kandambeth, S.; Biswal, B. P.; Chaudhari, H. D.; Rout, K. C.; Kunjattu, H. S.; Mitra, S.; Karak, S.; Das, A.; Mukherjee, R.; Kharul, U. K.; Banerjee, R. Selective Molecular Sieving in Self-Standing Porous Covalent-Organic-Framework Membranes. *Adv. Mater.* **2017**, *29*, 1603945.
48. Yuan, C.; Wu, X.; Gao, R.; Han, X.; Liu, Y.; Long, Y.; Cui, Y. Nanochannels of Covalent Organic Frameworks for Chiral Selective Transmembrane Transport of Amino Acids. *J. Am. Chem. Soc.* **2019**, *141*, 20187–20197.
49. Hao, Q.; Li, Z.-J.; Lu, C.; Sun, B.; Zhong, Y.-W.; Wan, L.-J.; Wang, D. Oriented Two-Dimensional Covalent Organic Framework Films for Near-Infrared Electrochromic Application. *J. Am. Chem. Soc.* **2019**, *141*, 19831–19838.
50. Yang, H.; Yang, L.; Wang, H.; Xu, Z.; Zhao, Y.; Luo, Y.; Nasir, N.; Song, Y.; Wu, H.; Pan, F.; Jiang, Z. Covalent Organic Framework Membranes through a Mixed-Dimensional Assembly for Molecular Separations. *Nat. Commun.* **2019**, *10*, 2101.
51. Zhao, Y.; Guo, L.; Gándara, F.; Ma, Y.; Liu, Z.; Zhu, C.; Lyu, H.; Trickett, C. A.; Kapustin, E. A.; Terasaki, O.; Yaghi, O. M. A Synthetic Route for Crystals of Woven Structures, Uniform Nanocrystals, and Thin Films of Imine Covalent Organic Frameworks. *J. Am. Chem. Soc.* **2017**, *139*, 13166–13172.
52. Shinde, D. B.; Sheng, G.; Li, X.; Ostwal, M.; Emwas, A.-H.; Huang, K.-W.; Lai, Z. Crystalline 2D Covalent Organic Framework Membranes for High-Flux Organic Solvent Nanofiltration. *J. Am. Chem. Soc.* **2018**, *140*, 14342–14349.
53. Fu, J.; Das, S.; Xing, G.; Ben, T.; Valtchev, V.; Qiu, S. Fabrication of COF-MOF Composite Membranes and Their Highly Selective Separation of H_2/CO_2. *J. Am. Chem. Soc.* **2016**, *138*, 7673–7680.
54. Li, Y.; Wu, Q.; Guo, X.; Zhang, M.; Chen, B.; Wei, G.; Li, X.; Li, S.; Ma, L. Laminater Self-Standing Covalent Organic Framework Membrane with Uniformly Distributed Subnanopores for Ionic and Molecular Sieving. *Nat. Commun.* **2020**, *11*, 599.
55. Sasmal, H. S.; Hader, A.; Kunjattu, H. S.; Dey, K.; Nadol, A.; Ajithkumar, T. G.; Bedaur, P. R.; Banerjee, R. Covalent Self-Assembly in Two Dimensions: Connecting Covalent Organic Framework Nanospheres into Crystalline and Porous Thin Films. *J. Am. Chem. Soc.* **2019**, *141*, 20371–20378.
56. Duan, C. H.; Majumdar, A. Anomalous Ion Transport in 2-nm Hydrophilic Nanochannels. *Nat. Nanotechnol.* **2010**, *5*, 848–852.
57. Huang, W.-L.; Wang, X.-D.; Ao, Y.-F.; Wang, Q.-Q.; Wang, D.-X. Artificial Chloride-Selective Channel: Shape and Function Mimic of the ClC Channel Selective Pore. *J. Am. Chem. Soc.* **2020**, *142*, 13273–13277.
58. Gillespie, D. High Energy Conversion Efficiency in Nanofluidic Channels. *Nano Lett.* **2012**, *12*, 1410–1416.
59. Vlassiouk, I.; Smirnov, S.; Siwy, Z. Ionic Selectivity of Single Nanochannels. *Nano Lett.* **2008**, *8*, 1978–1985.
60. Park, J.; Hinckley, A. C.; Huang, Z.; Chen, G.; Yakovenko, A. A.; Zou, X.; Bao, Z. High Temperature in a Zn-Based 3D Semiconductive Metal-Organic Framework. *J. Am. Chem. Soc.* **2020**, *142*, 20531–20535.
61. Brown, B. R. Sensing Temperature without Ion Channels. *Nature* **2003**, *421*, 495.
62. Chen, K.; Yao, L.; Su, B. Bionic Thermoelectric Response with Nanochannels. *J. Am. Chem. Soc.* **2019**, *141*, 8608–8615.
63. Li, Z.-Q.; Wu, Z.-Q.; Ding, X.-L.; Wu, M.-Y.; Xia, X.-H. A Solar Thermoelectric Nanofluidic Device for Solar Thermal Energy Harvesting. *CCS Chem.* **2020**, *2*, 2174–2182.
64. Zhang, P.; Chen, S.; Zhu, C.; Hou, L.; Xian, W.; Zuo, X.; Zhang, Q.; Zhang, L.; Ma, S.; Sun, Q. Covalent Organic Framework Nanofluidic Membrane as a Platform for Highly Sensitive Bionic Thermosensation. *Nat. Commun.* **2021**, *12*, 1844.